Applied Clay Science 291 (2026) 108274

Contents lists available at ScienceDirect

Applied Clay Science

journal homepage: www.elsevier.com/locate/clay

Research Paper

Probing structural changes of sepiolite and zeolitic water dynamics with temperature-dependent infrared spectroscopy and molecular simulations

Bidemi T. Fashina [a,b,*], Randall T. Cygan [a], Md Wasek Foysal [a], Youjun Deng [a,**]

[a] Department of Soil and Crop Sciences, Texas A&M University, College Station, TX 77843-2474, USA
[b] Geochemistry Department, Sandia National Laboratories, P.O. Box 5800-0754, Albuquerque, NM 87123, USA

ARTICLE INFO

Keywords:
Sepiolite/Palygorskite
Zeolitic water
Dehydration
FTIR spectroscopy
Molecular dynamics

ABSTRACT

Sepiolite, a hydrated magnesium silicate with tunnel-like structures, contains zeolitic water (H_2O), bound water (OH_2), and structural water (OH), which influence its thermal and structural properties. This study investigates the dehydration dynamics of sepiolite using in situ variable-temperature infrared (IR) spectroscopy (25–300 °C) and classical molecular dynamics (MD) simulations. The IR spectra reveal that most of the zeolitic water molecules (ν3375 cm^{-1} and δ1660 cm^{-1}) are lost at ~100 °C, and the residual zeolitic water molecules are lost at ~200 °C. Confinement in tunnels makes zeolitic waters more thermodynamically stable than surface-adsorbed waters (ν3252 cm^{-1}), which are completely lost by 100 °C. The gradual evacuation of the tunnel results in a shift in the stretching vibration of structural waters from 3690 to 3675 cm^{-1} due to diminished repulsion from the hydrogen atoms of zeolitic waters. The bound waters (ν3616, ν3565 and δ1625 cm^{-1}) are stable until 300 °C and subsequent loss induced the folding of layers. The MD simulations of a $4a \times 2b \times 10c$ supercell (Sep-8H_2O to Sep-0H_2O zeolitic water hydration states) show a ~ 1.2% tunnel height reduction upon dehydration, consistent with weakened Si–O–Si ribbons (1210 shifts to 1195 cm^{-1}). The zeolitic water molecules form 4, 3, and 2 structured layers in Sep-8H_2O, Sep-4H_2O, and Sep-2H_2O, respectively, with diffusion coefficients increasing from 5.0×10^{-10} m^2/s to 7.5×10^{-9} m^2/s as hydrogen bonding decreases. These findings elucidate the coordinated interplay of water types and structural changes in sepiolite, offering insights into its thermal stability and potential applications in catalysis and adsorption.

1. Introduction

The palygorskite-sepiolite group consists of 2:1 phyllosilicate clay minerals that exhibit modulated structures characterized by periodic inversion of Si tetrahedra every two pyroxene chains in palygorskite and three in sepiolite (Fig. 1a). This modulation forms nanoscale tunnels whose width is 10.60 Å (sepiolite), 6.40 Å (palygorskite), and height is ~3.7 Å for both minerals (Singer, 2002).

The ideal formula per half-unit cell is $Si_{12}Mg_8O_{30}(OH)_4(OH_2)_4{\cdot}xH_2O$ for sepiolite and $Si_8Mg_5O_{20}(OH)_2(OH_2)_4{\cdot}xH_2O$ for palygorskite. The formula indicates three types of water associated with the structures of both minerals. First is the OH — structural water which represents the hydroxyls coordinating with the Mg^{2+} in the octahedral sheet (i.e., Mg_3OH species) like in typical trioctahedral 2:1 layer silicates; second is the OH_2 — bound or coordination water to the Mg^{2+} at the edges/walls of the tunnels (i.e., $MgOH_2$ species); and the third type of water is the H_2O — zeolitic water in the tunnels (Brauner and Preisinger, 1956; Post et al., 2007).

Zeolitic water (Zw) molecules in sepiolite/palygorskite can influence the partitioning of molecules into the tunnel, often requiring partial dehydration to facilitate adsorption (Fois et al., 2003; Kuang et al., 2003; Giustetto and Chiari, 2004; Ovarlez et al., 2009; Tilocca and Fois, 2009; Dejoie et al., 2011; Karataş et al., 2017; Li et al., 2022). Furthermore, research on fluid properties under nanoconfinement indicates that, even without cations, confined fluids exhibit distinct properties and reactivity compared to their bulk counterparts — a phenomenon known as the confinement effect (Wang, 2014; Morikawa et al., 2015; Fumagalli et al., 2018; Ilgen et al., 2023). Thus, studying the dehydration of sepiolite and palygorskite surfaces and tunnels can elucidate the structure, dynamics, and reactivity of confined water in these minerals.

There have been several experimental and computational approaches to study surface and tunnel hydration and dehydration of

* Corresponding author at: Department of Soil and Crop Sciences, Texas A&M University, College Station, TX 77843-2474, USA.
** Corresponding author.
E-mail addresses: btfashi@sandia.gov (B.T. Fashina), yjd@tamu.edu (Y. Deng).

https://doi.org/10.1016/j.clay.2026.108274
Received 19 October 2025; Received in revised form 3 April 2026; Accepted 2 May 2026
Available online 29 May 2026
0169-1317/© 2026 Elsevier B.V. All rights are reserved, including those for text and data mining, AI training, and similar technologies.

sepiolite. Thermal and differential thermal approaches have been used to provide information on the water types, content, and thermodynamics, including thermal stability, dehydration/dehydroxylation steps, and associated enthalpies (Brauner and Preisinger, 1956; Serna et al., 1975; Sarikaya et al., 2000; Frost and Ding, 2003; Bukas et al., 2013; Hojati and Khademi, 2013; Yılmaz et al., 2013; Ogorodova et al., 2014). X-ray diffraction (XRD) has been instrumental in understanding crystallographic transformations, unit cell parameters, and phase changes during hydration, dehydration and dehydroxylation (Brauner and Preisinger, 1956; Nagata et al., 1974; García-Romero et al., 2007; Post et al., 2007; Fashina and Deng, 2022). Being sensitive to specific bond vibrations, Fourier transform infrared spectroscopy (FTIR) provides molecular-level information complementary to structural (XRD) and mass/energy (thermogravimetric analysis, microcalorimetry, etc.) changes during the dehydration of sepiolite (Sarikaya et al., 2000; Frost and Ding, 2003; Bukas et al., 2013; Tsampodimou et al., 2015). Nuclear Magnetic Resonance (NMR) spectroscopy, particularly solid-state NMR, provides unique atomic-level insights into the hydration states of sepiolite (Weir et al., 2002) and the structural changes associated with the hydration and dehydration of sepiolite (Facey et al., 2005; Ogorodova et al., 2014). The hydration and dehydration of sepiolite not only cause changes to the framework but also to the arrangement and distribution of the Zw molecules. Through Rietveld refinement of synchrotron powder XRD data and molecular dynamics (MD) simulation, insights have been gained into the sites of zeolitic waters in the tunnel of sepiolite for fully hydrated and fully dehydrated phases (Post et al., 2007; Zhou et al., 2016). Results from near-infrared experiments suggest that there is at least one intermediate state during the zeolitic dehydration of sepiolite tunnels (Bukas et al., 2013). Hence, the dehydration of the tunnel is a step process which involves continuous re-organization and re-distribution of zeolitic waters.

This study investigates structural changes of sepiolite and zeolitic water dynamics through a combination of experimental and computational approach. In situ heating experiments monitored subtle changes to the infrared bands of sepiolite to elucidate the impact of dehydration on the structure and thermodynamics of sepiolite. Given the complexity of studying confined fluids — due to overlapping electrical double layers (EDLs) from opposing surfaces (Mg–OH_2 on tunnel sides and Si—O on top/bottom; Fig. 1a) — molecular dynamics simulations were employed to determine the contribution of each surface to the structure, dynamics, and distribution of zeolitic water across hydration states.

2. Materials and methods

2.1. Sample preparation

The sepiolite sample was from the Cabañas de la Sagra mine located in the municipality of Cabañas de la Sagra, province of Toledo, central Spain. It was collected by one of the authors (Y. Deng) on a field trip organized at the 2010 SEA-CSSJ-CMS Trilateral Meeting on Clays (Seville, Spain). The sepiolite is a Middle Miocene lacustrine–palustrine precipitate formed in evaporitic, Mg-rich shallow basins of the central Tagus (Tajo) Basin (Delgado et al., 1977; Lomoschitz et al., 1985). This sample was used in our earlier study (Fashina and Deng, 2022), the in situ XRD pattern during heating and the EDS spectrum of the specimen were reported there. It is relatively pure sepiolite sample with minimum amount of mica. The sample was also characterized by simultaneous thermal analysis (TGA/DSC) on a TA Instruments Discovery SDT 650. The TGA/DSC analysis was performed under N_2 atmosphere between 25 and 500 °C at temperature increment of 10 °C/min (See SI). The Scanning Electron Micrograph of the sepiolite sample shows elongated fibrous morphology with bundled and intertwined needle-like laths (See SI). The Si:Mg ratio of ~1.48, which is very close to the ratio of 1.5 shown in the ideal formula, and Si:Al ratio of ~19.25 (Fashina and Deng, 2022) confirmed a rounded structural formula of $Si_{12}(Mg_{7.4},Al_{0.6})O_{30}(OH)_4(OH_2)_4{\cdot}xH_2O$. This is the formula expected for near-ideal and high-purity sepiolite with minimal substitution (Frost et al., 2001; Post and Heaney, 2008; García-Romero and Suárez, 2010). The sepiolite was treated with sodium acetate buffer solution to remove carbonates and with dithionite-citrate-bicarbonate to remove iron oxide minerals. The <2 μm fraction of sepiolite was separated from the bulk by centrifugation. The sample was previously characterized by using in situ variable-

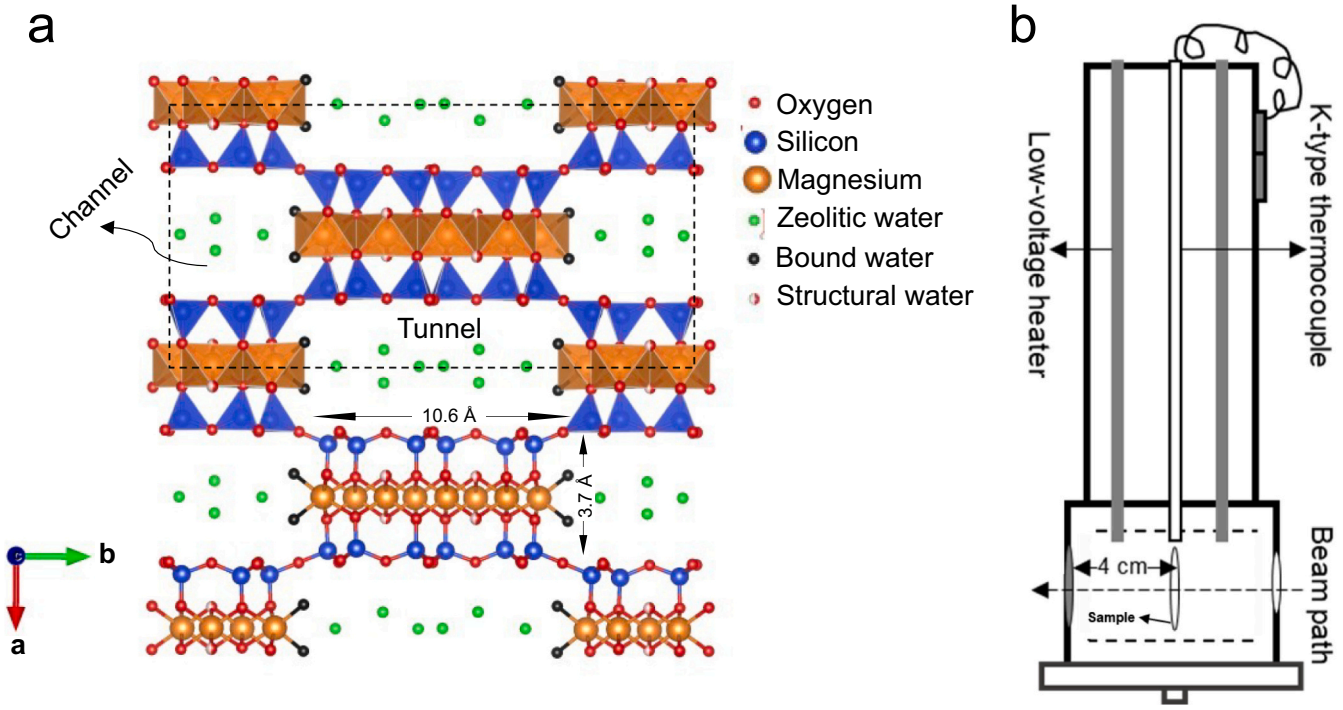

Fig. 1. (a) Polyhedral (top) and ball and stick (bottom) models of sepiolite (Brauner and Preisinger, 1956) viewed along tunnel direction, and (b) a schematic of the Dewar transmission/reflection accessory.

temperature XRD and thermogravimetric analysis (Tsampodimou et al., 2015; Fashina and Deng, 2022).

2.2. Variable temperature infrared spectroscopy

About 0.1 mL of sepiolite dispersion (5 mg/mL) was pipetted on a 32 × 2 mm ZnS disc (International Crystal Laboratories, Garfield, New Jersey, United States) and left to air-dry for 24 h. The dried film was stored for 48 h at 22 °C under an atmosphere of ~100% relative humidity. Infrared spectra were recorded between 4000 and 800 cm^{-1} at a resolution of 2 cm^{-1} as the average of 32 scans on a Perkin Elmer Spectrum 100 Fourier-transform infrared spectrometer (FTIR; Perkin Elmer, Waltham, Massachusetts, USA). The Dewar transmission/reflection accessory (Harrick Scientific, New York, USA) was mounted on the spectrometer for in situ variable temperature dehydration of sepiolite (Fig. 1b). The temperature was monitored with the Harrick ATC-024-2 temperature controller. The spectra were acquired between 25 and 300 °C while allowing a dwell time of 5 min at each temperature interval before spectra were acquired. The infrared spectra of the supporting ZnS disc were recorded at the same temperatures to be used as the blanks at the corresponding temperatures. We checked the FTIR pattern of the ZnS after 400 °C heating, and observed no new bands compared to the unheated ZnS disc, suggesting the changes in the recorded infrared spectrum were not due to the oxidation, if any, of the ZnS disc itself.

For post-processing of the infrared spectra, the blank spectrum of the ZnS disc was subtracted from the sample spectrum followed by the deduction of the empty blank at corresponding temperatures (i.e., the spectrum of the ambient surroundings). The former allows the correction for impurities and artifacts (e.g., background) while the latter corrects for the contributions from the environment (e.g., moisture, etc.). The difference calculation was performed in the absorbance scale because it has a linear relationship with concentration and path length. The resulting spectrum is mildly smoothed such that the spectral features of interest are not altered. The difference calculation and the Savitzky-Golay smoothing algorithm were implemented in the Spectrum 10 software (Perkin Elmer, Waltham, Massachusetts, USA).

2.3. Classical molecular dynamics

2.3.1. Structural models and force fields

The starting structure was a unit cell of sepiolite with lattice constants $a = 13.405$ Å, $b = 27.016$, $c = 5.275$, and $\alpha = \beta = \gamma = 90.00°$ (Post et al., 2007). The formula for an ideal half unit cell of sepiolite is $Si_{12}Mg_8O_{30}(OH)_4(OH_2)_4{\cdot}xH_2O$, where x can vary between 0 (zeolitically dry) and 8 (~ 100% zeolitically hydrated) depending on experimental conditions (Post et al., 2007; Bukas et al., 2013). To model the structure and organization of the Zw molecules in the tunnels of sepiolite, the ideal unit cell of sepiolite was expanded to a $4a \times 2b \times 10c$ supercell. Each tunnel in a half-unit cell has 8 Zw molecules and 4 Bw molecules making a total of 1920 water molecules. The supercell has 15,040 atoms (Table 1) and lattice parameters of $a = 53.62$ Å, $b = 53.03$ Å, $c = 52.75$ Å, and $\alpha = \beta = \gamma = 90.00°$, representing the fully hydrated sepiolite. To generate structures at various zeolitic hydration/dehydration states: two, four, six, and eight Zw molecules (from each half unit cell) were randomly removed from the fully hydrated tunnel. Hence, a total of four structures were generated, differing in the number of zeolitic water molecules — 8, 4, 2, and 0 per tunnel, and are denoted as Sep-8H_2O, Sep-4H_2O, Sep-2H_2O, and Sep-0H_2O, respectively (see SI and Table 1.). Editing and visualization of the starting models were implemented in Material Studio, Ovito, and *V*esta (Stukowski, 2009; Momma and Izumi, 2011; BIOVIA, 2018). A list of abbreviations used within the text is given in Table 2.

Table 1
The number and types of water molecules for each zeolitic hydration state of the 4 × 2 × 10 cells.

	H_2O	OH_2	Total water	Total atoms
Sep-8H_2O	1280	640	1920	15,040
Sep-4H_2O	640	640	1280	13,120
Sep-2H_2O	320	640	960	12,160
Sep-0H_2O	0	640	640	11,200

H_2O = zeolitic water and OH_2 = bound/coordinated water.

The forcefield parameters for water were in accordance with the flexible SPC water model and sepiolite with Clayff, respectively (Teleman et al., 1987; Cygan et al., 2004, 2021). Following Clayff, all the atoms were non-bonded except for the three waters – H_2O (Zw), OH_2 (Bw), and OH (Sw). Similarly to Ockwig et al. (2009), the only modification to Clayff was the charge assignment for the Mg^{2+} atoms at the edge of the tunnel ($MgOH_2$) which were adjusted to +1.620 e (where e is the elementary charge) to maintain neutral models.

2.3.2. Simulation methods

Structural models were optimized using the conjugate gradient algorithm (Ford, 2015) followed by a microcanonical *NVE* ensemble (constant number of atoms *N*, constant volume *V*, and constant Energy *E*) of the models at 300 K for 1 ns using a 1 fs timestep to equilibrate the structures. Two canonical *NVT* ensemble (constant temperature *T*) runs were each conducted at 300 K for 2 ns while damping (relaxing) the temperature at 100 timesteps. Finally, two isothermal-isobaric *NPT* ensembles (constant pressure *P*) were performed at 1 atm and 300 K for 2 ns each at 1 fs timestep. In both the *NVT* and *NPT* runs, the first runs were to maintain stable temperature and pressure while the second runs were the production runs. Temperature and pressure were controlled using a Nosé-Hoover thermostat and barostat (Shinoda et al., 2004).

From the production runs, the (i) number of H-bonds (N_{H2O}) and the H-bond lengths (L_{H2O}) were calculated based on geometric constraints — angle and distance (See SI), (ii) one-dimensional self-diffusion coefficient, *D*, in the *z* plane (Cygan and Kubicki, 2001), (iii) radial distribution functions (RDF) (Allen and Tildesley, 2017), atomic density profiles (ADP) were plotted using Mg atoms on the edge/walls of the tunnel and basal oxygen atoms of the tetrahedral sheet of the top/bottom of the tunnel as reference atoms for the ADP along the *b*- and *a*-axis, respectively.

3. Results and discussion

3.1. Variable temperature infrared spectroscopy

3.1.1. Silanols

The silanol groups (Si–OH) are terminal groups located on the tetrahedral sheets terminating the channels. The Si–OH are not observed at room temperature because sepiolite retains an abundant amount of external surface water which can mask or interfere with the infrared signals of silanol groups due to hydrogen bonding with adsorbed or

Table 2
Description of the abbreviations in the text.

Abbreviations	Description
S_w	Structural water (OH)
B_w	Bound water $(OH)_2$
O_b	Oxygen atom of bound water
H_b	Hydrogen atoms of bound water
H_{b1}	The hydrogen close to the top/bottom of the tunnel
H_{b2}	The hydrogen in the middle of the tunnel
O_h	The oxygen of the structural waters
Z_w	Zeolitic water
H_z	Hydrogen atom of zeolitic water
O_z	Oxygen atoms of zeolitic water
O	Oxygen at the top/bottom of the tunnel
H_w	$H_b + H_z$
O_w	$O_b + O_z$
O_f	The oxygen atoms in the octahedral sheet

zeolitic water molecules present in the channels at room temperature. Hence, silanol groups become more distinguishable in infrared spectra when sepiolite is heated or degassed to remove surface adsorbed waters (Tsampodimou et al., 2015). In this study, the silanol band (ν3720 cm^{-1}) appears at ≥50 °C and remains stable up to <300 °C (Fig. 2a). The band split into three bands at about 3730, 3723, and 3716 cm^{-1} when the sample was heated to ≥250 °C, which was because of the folding of the structure that changes the distance of the silanol groups to the surfaces they are approaching. Splitting of the silanol overtone band at 7270 cm^{-1} into 7307, 7283, and 7264 cm^{-1} has been reported (Tsampodimou et al., 2015).

3.1.2. Zeolitic water and external water

The stretching vibrations of Zw and adsorbed water appear at 3375 cm^{-1} and 3252 cm^{-1}, respectively, with their bending vibrations producing a broad band at 1660 cm^{-1} (Fig. 2a and Table 3) (Shuali et al., 1989; Bukas et al., 2013). Between 25 and 100 °C, the ν3252 cm^{-1} disappeared indicative of the complete loss of physisorbed waters. Most of the zeolitic water molecules were also gone at ≤100 °C but a small broad peak (~3400 cm^{-1}) showed up at >100 °C. This might be indicative of a more stable zeolitic water molecule that is less H-bonded. This new band did not completely disappear until >200 °C. This is suggestive that, on average, the physisorbed waters are less stable than the zeolitic waters. This is in agreement with earlier calorimetric results for sepiolite, which indicate that Zw are more thermodynamically stable compared to the physisorbed waters (Frost and Ding, 2003; Ogorodova et al., 2014). The TGA data align with the IR observations, showing that most adsorbed and zeolitic water is lost by ~100–150 °C, contributing a weight loss of approximately 8% in this range (see SI).

3.1.3. Bound water

The bound water (OH_2) produced bands at 3616 cm^{-1} and 3565 cm^{-1} (O—H stretching modes of Mg–OH_2) and 1625 cm^{-1} (O—H bending mode) (Fig. 2 and Table 3). The two stretching bands arise from differing H-bonding strengths within a single Bw molecule: O-H_{b1}, the strongly H-bonded to the basal surfaces of the tunnel (top/bottom), produces the 3565 cm^{-1} band, while O-H_{b2}, with weaker H-bonding, corresponds to 3616 cm^{-1} (Fig. 3a) (Frost et al., 2001; Madejová, 2003). Hence, the 3616 cm^{-1} is from less-perturbed O-H_{b2} and 3565 cm^{-1} the strongly perturbed H-bonded O-H_{b1}, respectively. The variation of the O-H_{b2} band between 3616 and ~ 3640 cm^{-1} among sepiolite specimens (Ahlrichs et al., 1975; Serna and Vanscoyoc, 1979; Shuali et al., 1989; Post and Crawford, 2007; Mora et al., 2010; Hojati and Khademi, 2013) has led to the assignment of the band as the O—H vibration of dioctahedral-like Mg_3OH species (Frost et al., 2001; Mora et al., 2010). Indeed, the 3616 cm^{-1} band is characteristic of Al_2OH of dioctahedral systems like palygorskite (Russell and Fraser, 1994; Gionis et al., 2006). Other dioctahedral minerals like kaolinite and montmorillonite have this band around 3620 cm^{-1} as well. However, in situ deuteration at ambient conditions confirms the 3616 cm^{-1} band is the O—H vibration of Bw (Bukas et al., 2013). Also, the earlier acquired energy dispersive spectrum of this sample did not suggest a strong dioctahedral character (Fashina and Deng, 2022).

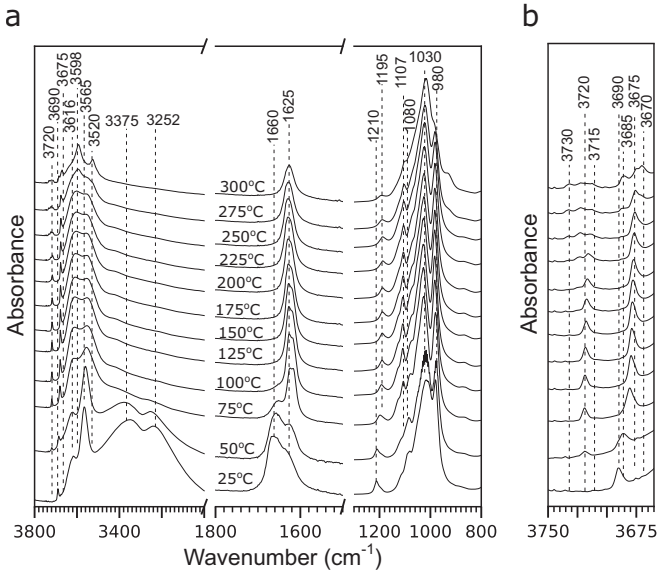

Fig. 2. In situ variable temperature infrared spectrum of sepiolite. The intensities of the three panels were multiplied by 1.5 (left and middle panel) and 0.3 (right panel) for clarity.

Despite the loss of most of the Zw molecules, the 3616 cm^{-1} (O-H_{b2}) peak positions were maintained except for peak broadening. This suggests that most of the Zw molecules are not strongly associated with Bw because the loss of Zw should shift the O-H stretching band of the Bw to higher wavenumbers. At ≥200 °C, the peak gradually became more intense, and the position shifted to 3600 cm^{-1}. Between 75 and 275 °C, the 3565 cm^{-1} peak became broader and shifted to 3520 cm^{-1} and another shift at 300 °C to a sharp peak at 3520 cm^{-1}. This indicates a stronger H-bond interaction between the H_{b1} and the O atoms at the top/bottom of the tunnel. Stronger interaction is made possible because the height of the tunnel slightly collapsed on evacuating most of the zeolitic waters. Post et al. (2007) observed about 1.2% shrinkage in the height of sepiolite tunnel after complete loss of zeolitic water.

At 300 °C, the intensity of the bending vibration of water reduced by almost half because of the loss of half of the Bw per edge Mg. The TGA data also indicate an additional ~3.5–4% weight loss between 250 and 300 °C, which is consistent with the theoretical mass loss of approximately 3.3% expected for the removal of half the bound water molecules from the formula $Si_{12}(Mg_{7.4},Al_{0.6})O_{30}(OH)_4(OH_2)_4{\cdot}xH_2O$ (see SI). The loss of half of the Bw induces the Mg to form a bond with the basal oxygen so as to complete octahedral coordination (Lokanatha and Bhattacheijee, 1985; Post et al., 2007). This in turn drives the structure of sepiolite to fold (Fig. 3b). Similar to the unfolded and zeolitically hydrated structure (Fig. 3a), the residual Bw has two O—H stretching modes. The bands manifest at 3598 and 3530 cm^{-1}, which correspond to the stretching vibrations of O-H_{b1} and O-H_{b2} that are H-bonded to the basal oxygens of the folded sepiolite structure at different distances (Fig. 3b). It is worth noting that the loss of the two Bw at different temperatures does not imply differences in the thermodynamic stability of both waters. An explanation for the difference might be that the Bw that is first lost depends on the direction of fold (i.e., top or bottom). If the fold is from the top layer, the top Bw is destabilized by the basal surfaces while the bottom Bw is less impacted (Fig. 3b).

3.1.4. Structural OH

The assignment of the 3690 cm^{-1} band to O—H stretching vibration to Mg_3OH species is well accepted (Hayashi et al., 1969; Bukas et al., 2013). This band position is considerably higher than the 3676–3678 cm^{-1} for fully trioctahedral clay minerals such as hectorite, talc, and saponite (Farmer and Russell, 1964; Petit et al., 2004; Wu et al., 2022). The band linearly (with temperature increase) shifts to 3678 cm^{-1} (Fig. 2b and Fig. 4a). The linearity occurs up to about 100 °C, after which the band remained constant up to 200 °C. To the best of our knowledge, this is the first time such a systematic shift (as a function of temperature) has been reported. After 200 °C, the band dropped to 3675 cm^{-1} and remained constant up to 275 °C. Above 275 °C, the intensity of the ~3675 cm^{-1} band reduced by about 50% while two new peaks emerged at about 3685 and 3670 cm^{-1} (Fig. 2b). This suggests that at 300 °C, there are three components all corresponding to the O—H stretching vibration of the octahedral sheet (i.e., Mg_3OH species): (i) 3675 cm^{-1} – from unfolded sepiolite layers, (ii) 3685 cm^{-1} – from the folded sepiolite layers where half of the Mg_3O–H in the folded layer is perturbed by the H_{b1} of the residual Bw (i.e., H_{b1}–OH_1 repulsion in Fig. 3b) similar to the

Table 3
Peak assignment for the observed bands during the in situ heating of sepiolite assignment for the observed bands during the in situ heating of sepiolite.

Temp (°C)	Band assignment in response to temperature (cm^{-1})										
	ν(SiO − H)	ν(Mg_3O − H)	ν(MgO − H_2)	ν(MgO − H_2)	ν(O − H)		δ(O − H)		δ(MgO − H_2)	ν(Si − O − Si)	ν_{as}(Si − O)
					Z_w	S_w	Z_w	S_w			
25	–	3690	3616	3565	3375	3250	1660	1660	1625	1210	1080
50	3720	3686	3616	3565	3375	3250	1660	1660	1625	1210	1080
75	3720	3680	3616	3545	3375	3250	1660	1660	1625	1195	1080
100	3720	3679	3616	3545	3375	3250	–	–	1625	1195	1195
125	3720	3678	3615	3545	3375	3250	–		1625	1210	1195
150	3720	3678	3615	3545	3375	3250			1625	1210	1195
175	3720	3678	3613	3545	3375	3250			1625	1208	1195
200	3716	3678	3612	3545	3375	3250			1625	1206	1195
225	3716, 3723	3675	3607	3545	3375	3250			1625	1202	1195
250	3716, 3723, 3730	3675	3607	3545	3375	–			1625	1198	1195
275	3716, 3723, 3730	3675	3598	3520	3375	–			1625	1196	1195
300	3716, 3723, 3730	3685, 3675, 3670	3598	3520	3375	–			1625	1194	1195

ν: Stretching vibration; δ: Bending vibration; ν_{as}: Antisymmetric stretching vibration; −: Band not observed or absent.

repulsive effect by the zeolitic water leading to a band at 3690 cm^{-1} and (iii) 3670 cm^{-1} – from the folded sepiolite layers where half of the Mg_3O–H in the folded layer not impacted by the residual Bw (i.e., OH_2 in Fig. 3b).

The observed response of the structural water (i.e., OH) to temperature/moisture conditions is unusual considering that other trioctahedral clay minerals do not show this response. The only exception is when the O—H is perturbed by a cation closely adsorbed in the ditrigonal hole of saponite or due to octahedral substitution in talc (Pelletier et al., 2003; Petit et al., 2004). As earlier mentioned, the energy dispersive spectrum of the specimen does not suggest octahedral substitution or the presence of counter ions in the tunnel (Fashina and Deng, 2022). Given the observed red shift, H-bonding of the structural waters to surface water cannot be the reason for the observed response to temperature. Instead, the red shift is likely due to the loss of zeolitic waters in the tunnel of sepiolite. As will be shown later by computational methods, the waters in the tunnel have their hydrogen atoms pointing towards the basal surfaces, which will in turn repel the hydrogen atoms of the structural water allowing the O − H bond to be less perpendicular (i.e., more parallel) to the surface. Being neutral, the basal surfaces do not screen the charges. Hence, the O − H stretching vibration of the Mg_3OH registers at 3690 cm^{-1}. The repulsion reduces as zeolitic waters are lost, making the peak shift from 3690 cm^{-1} (25 °C) to 3685 cm^{-1} (50 °C) and then 3678 cm^{-1} (100 and 200 °C). Also, Fig. 4a of our study is similar to Fig. 7 in Post et al. (2007) (plot of total number of zeolitic water molecules vs temperature), indicative of a direct correlation between the Mg_3O–H stretching *v*ibration and the number of zeolitic waters in the tunnel.

3.1.5. Siloxane linkages

The stretching vibration of the Si-O-Si linkages (Fig. 4b) between the ribbons of the modulated 2:1 layer is observed at 1210 cm^{-1} (Russell and Fraser, 1994; Perraki and Orfanoudaki, 2008; Bukas et al., 2013; Hojati and Khademi, 2013). The position and the sharpness of the peak also suggests high crystallinity of this sepiolite sample (Frost et al., 2001). This band is stable up to 50 °C but begins to shift to a lower wavenumber (1195 cm^{-1}) (Fig. 4b). This agrees with in situ variable temperature XRD experiments where the *110* reflection of sepiolite shifted from 12.05 Å (ambient condition) to 11.95 Å (~300 °C) confirming the shrinking of the crystal lattice (Fashina and Deng, 2022). Similar magnitude of shrinkage was observed for palygorskite (shift from 10.50 Å to 10.30 Å between 30 °C and 250 °C). Herein, the shift to the lower wavenumber indicates the weakening/elongation of the Si-O-Si, which leads to a reduced tunnel height as the modulated tetrahedral-octahedral-tetrahedral structure begins to collapse into the tunnel as zeolitic waters are lost causing a strain (weakening) of the Si-O-Si linkages.

3.1.6. Other Si—O bonds

A Si—O stretching vibration is observed at 1080 cm^{-1}. From 200 °C, the intensity of the absorbance band begins to reduce until 300 °C where it fully disappears. A new absorbance band emerges at 1107 cm^{-1}. This is consistent with Bukas et al. (2013) where a 1082 cm^{-1} absorbance band was observed at ambient conditions but shifted to 1108 cm^{-1} when the sample was dried. Other Si—O modes include a ~ 1005 cm^{-1} which shifted to 1030 cm^{-1} upon heating which is assigned to the Si–O–Si antisymmetric stretching vibration primarily associated with the tetrahedral sheet (Frost et al., 2001). In the unheated sample, the Si—O bond in the tetrahedral sheets is weakened by hydrogen bonding interactions with the abundant zeolitic water while heating removes the zeolitic water molecules which strengthens the Si—O bonds. Another Si—O mode is at 980 cm^{-1} which gradually lost intensity during heating to finally disappear at 300 °C. This agrees with the extrapolations of Bukas et al. (2013) that estimated these absorbance bands to be at 1018 and 975 cm^{-1} at ambient conditions and 1023 and 977 cm^{-1}, respectively, upon drying.

3.2. Computational data

3.2.1. Lattice constants

Snapshots of structural models resulting from the *NPT* MD simulations (Fig. 5 and SI). The crystallographic parameters (Table 4) agree with previous experimental and computational studies (Post et al., 2007; Ockwig et al., 2009). There was no change in the *b*- or c- axis during simulation of zeolitic dehydration. There is a minor change in the *a*-axis as the model was zeolitically dehydrated. Between Sep-8H_2O and Sep-0H_2O the *a*-axis shrank by ~1.2% which is in perfect agreement with Post et al. (2007) observation of a shrinkage of ~1.2% along the height of the tunnel. As indicated by the results of the in situ infrared (> 50 °C), the reduction in the height of the tunnel is due to the weakening of the Si-O-Si linkages (Fig. 2a and Fig. 4b) as the tunnel is evacuated.

3.2.2. Structure and arrangement of zeolitic water, bound water, and structural OH

The ADP of each zeolitic water molecules was monitored along the height and width of the tunnel to elucidate the structure and distribution of zeolitic waters in either direction for the equilibrated simulation. Overall, the structure of the zeolitic water was more defined along the width of the tunnel compared to the height of the tunnel (Figs. 6 and 7).

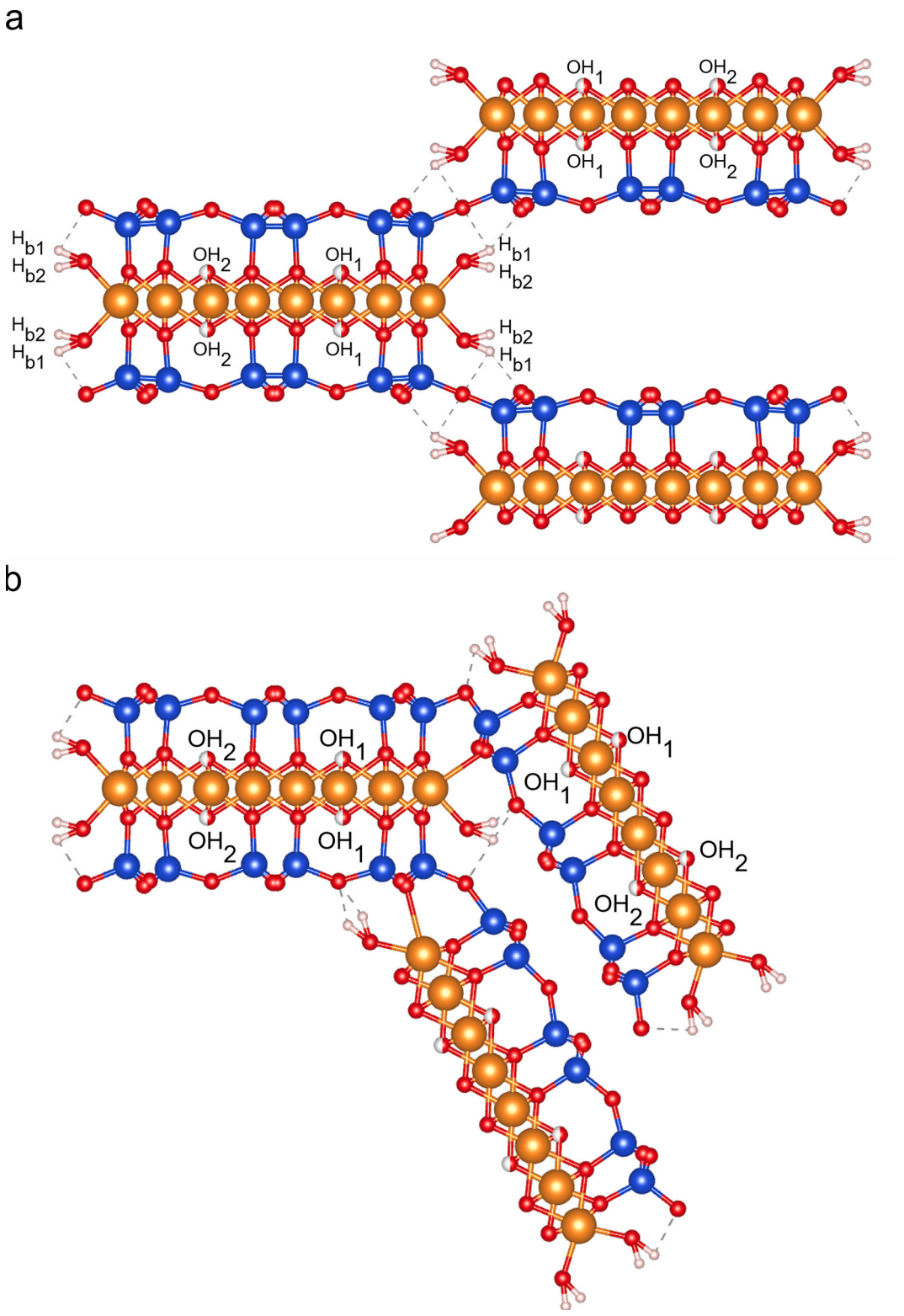

Fig. 3. Ball and stick model of sepiolite representing (a) unfolded and (b) folded layers. The zeolitic waters in the unfolded model are not shown for clarity.

3.2.2.1. Bound water. For the hydrated states (i.e., $n = 8$–2), in contrast to the common pictorial depictions in the literature, the O_b is asymmetric along the height of the tunnel (i.e., between the two H_b) but closer to the H_{b2} (Fig. 6) because of electrostatic attraction of H_{b1} to the basal oxygens lining the top/bottom of the tunnel. The difference in distance leads to two types of O − H stretching vibration by bound water, which is consistent with the experimental data that the stretching vibration of bound water is found to have two band positions — 3616 and 3565 cm^{-1}. Comparing Sep-8H_2O and Sep-2H_2O, the structure of the bound water was not significantly perturbed. This agrees with the IR

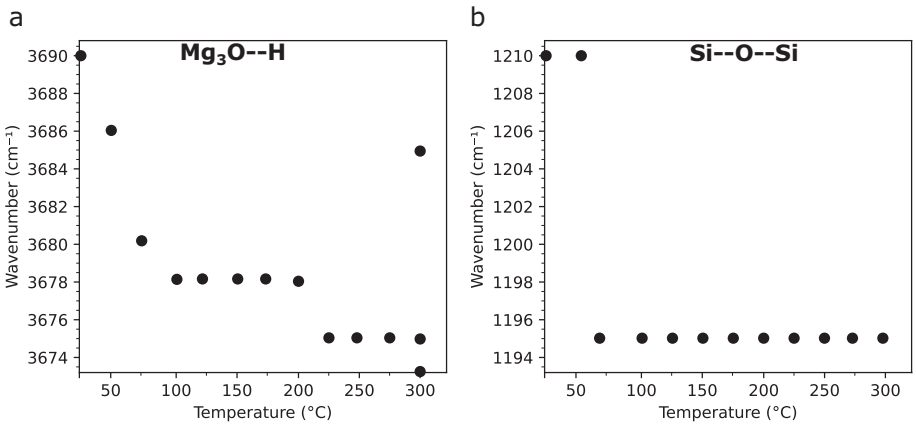

Fig. 4. Plots of the stretching vibration of the (a) O—H and (b) Si-O-Si linkers in response to temperature.

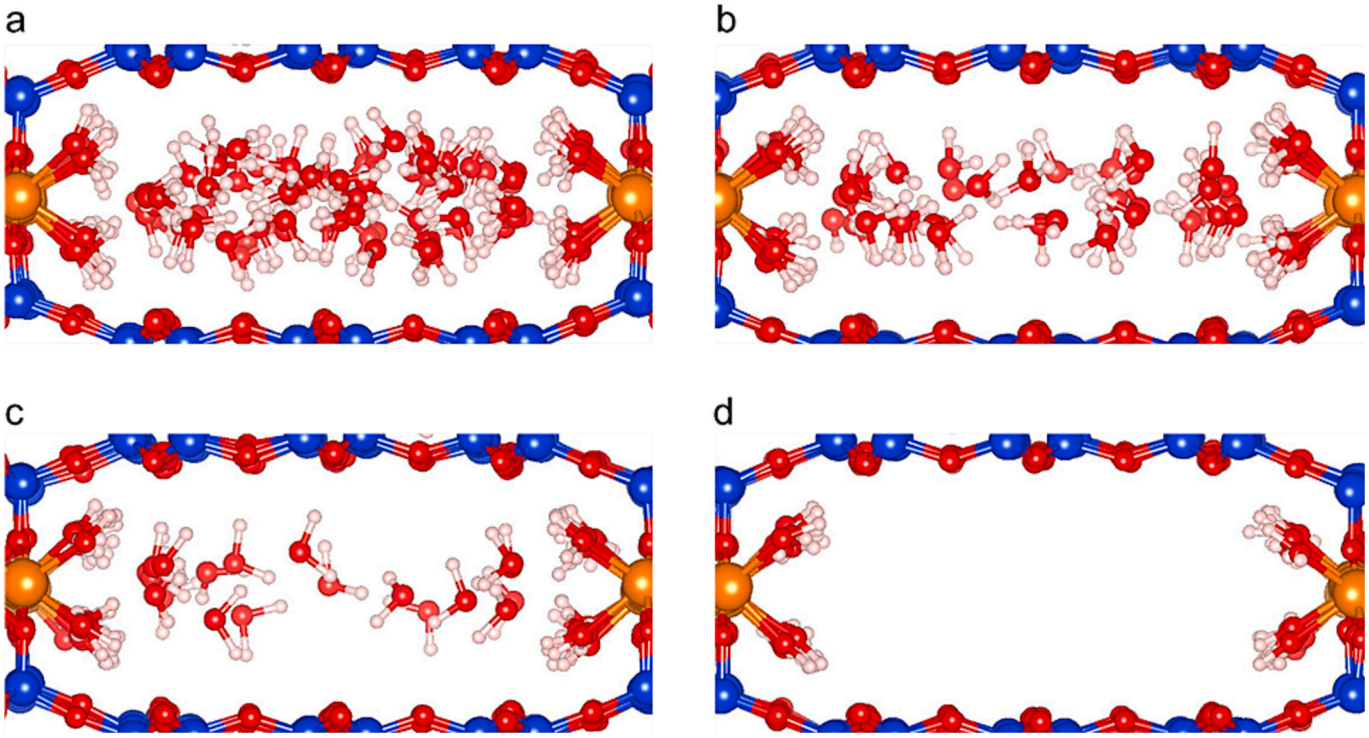

Fig. 5. Snapshot of the distribution of zeolitic water in the tunnel of sepiolite for models (a) Sep-8H_2O, (b) Sep-4H_2O, (c) Sep-2H_2O, and (d) Sep-0H_2O.

Table 4
Unit cell parameters of sepiolite, number of hydrogen bonds per zeolitic water (N_{H2O}), and hydrogen bond length (L_{H2O}) between zeolitic waters in sepiolite at different zeolitic hydration states.

	Unit cell parameters				H-bonds	
	a (Å)	*b* (Å)	*c* (Å)	*α*, *β*, *γ*	N_{H2O}	L_{H2O}((Å)
Start	13.405	27.016	5.275	90		
Sep-8H_2O	13.24 ± 0.06	26.87 ± 0.03	5.23 ± 0.02	90	1.02	2.82
Sep-4H_2O	13.06 ± 0.06	26.90 ± 0.02	5.23 ± 0.02	90	0.66	2.86
Sep-2H_2O	13.04 ± 0.07	26.92 ± 0.02	5.23 ± 0.02	90	0.43	2.87
Sep-0H_2O	13.08 ± 0.07	26.93 ± 0.02	5.23 ± 0.02	90	0	–
Expt	13.405	27.016	5.275	90		

The *a*, *b*, and *c* dimensions are per unit cell; N_{H2O} is the average of H-bonds normalized to the number of zeolitic waters (i.e., total number of H-bonds/Number of zeolitic water); L_{H2O} is the average length of H-bonds; Expt. = experimentally (Post et al., 2007). Note: The standard deviation of L_{H2O} ranged between 5 and 6% of the mean values.

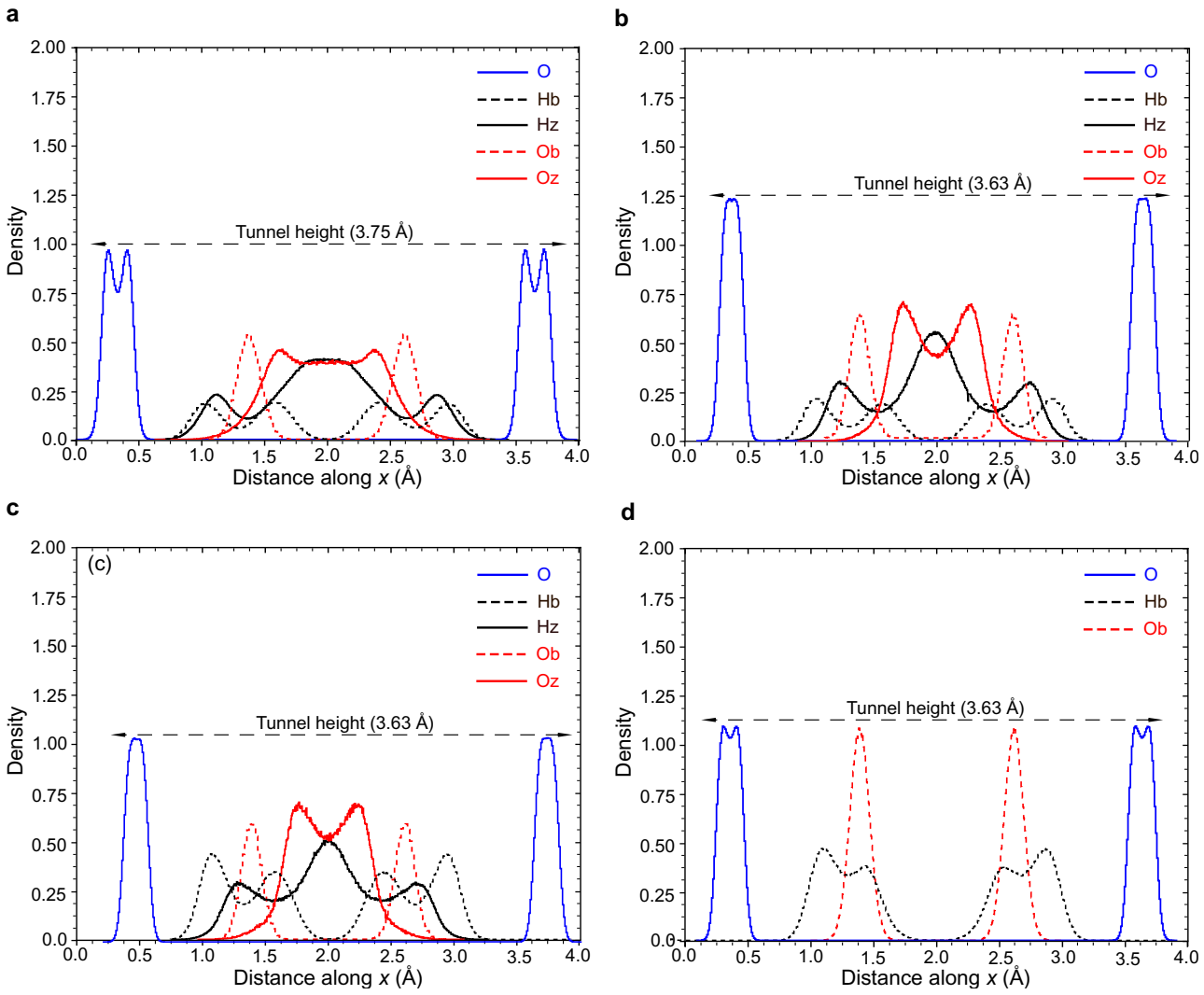

Fig. 6. The atomic density *a*-profile of (a) Sep-8H_2O, (b) Sep-4H_2O, (c) Sep-2H_2O, and (d) Sep-0H_2O. See Table 2 for the description of the abbreviations.

data where the stretching and bending vibration of the bound water is invariant until 300 °C (Fig. 2). However, at Sep-0H_2O, the bound water assumes a different structure from the earlier zeolitic states. The difference is that H_{b2} now has shorter distances along and across the tunnel. The H_{b2} now almost coincides with O_b both along and across the tunnel. Perhaps, this structure allows for the bound water in one tunnel to form an H-bond with the bound water of the next tunnel. Overall, there seem to be two possible structures of bound water: Type 1 is characteristic of the first three zeolitic states (i.e. Sep-8H_2O, Sep-4H_2O, and Sep-2H_2O) while Sep-0H_2O has Type 2 (Fig. 5).

3.2.2.2. Zeolitic water. The structure of the zeolitic water is less defined across the tunnel compared to along the tunnel (Figs. 6 and 7). Along the tunnel, in the Sep-8H_2O model, the only structured layer of water is the water close to the top/base of the tunnel while the water in the middle of the tunnel is less structured and resembles bulk water. On losing two and four zeolitic waters per half unit cell, the middle region becomes more structured while the structured zeolitic water close to the basal surfaces becomes more organized and moves closer to the middle of the tunnel. Across the tunnel, the structure of water is more defined. To determine the number of zeolitic states and their distribution, we extracted and averaged the *x* and *y* positions of the atoms of zeolitic waters in the tunnels. There are 4, 3, and 2 zeolitic layers of water on each side of the tunnel for Sep-8H_2O, Sep-4H_2O, and Sep-2H_2O, respectively (Fig. 8). But the number of H-bonds decreased while the length increased per zeolitic water molecule, resulting in a linear correlation of 99% (Table 4).

1. *Sep-8H_2O* — The occurrence of four sites in the fully hydrated state (Fig. 8a) agrees with the synchrotron and Rietveld data (Post et al., 2007) and the computational results of Zhou et al. (2016) but different from the earlier proposed three-site model (Brauner and Preisinger, 1956). Also, the distribution of these sites in the tunnel is different from what was earlier observed in MD calculations (Zhou et al., 2016) or Rietveld analysis (Post et al., 2007). The difference between our results and earlier MD calculations is understandable since the former authors computed (i) the distribution of zeolitic sites from ADF along the width of the tunnel only and (ii) zeolitic sites from a histogram of all oxygen atoms in the tunnel making it difficult to ascertain the positions of the bound and zeolitic states especially in the fully zeolitically hydrated states. In the current study, both pitfalls were avoided. In addition to the four zeolitic sites along the tunnel, there are also two zeolitic sites across the tunnel for Sep-8H_2O (Fig. 8a). Both are needed to determine zeolitic sites within the tunnel. The first zeolitic site (Zw_1) is coordinated with H_{b2} while the

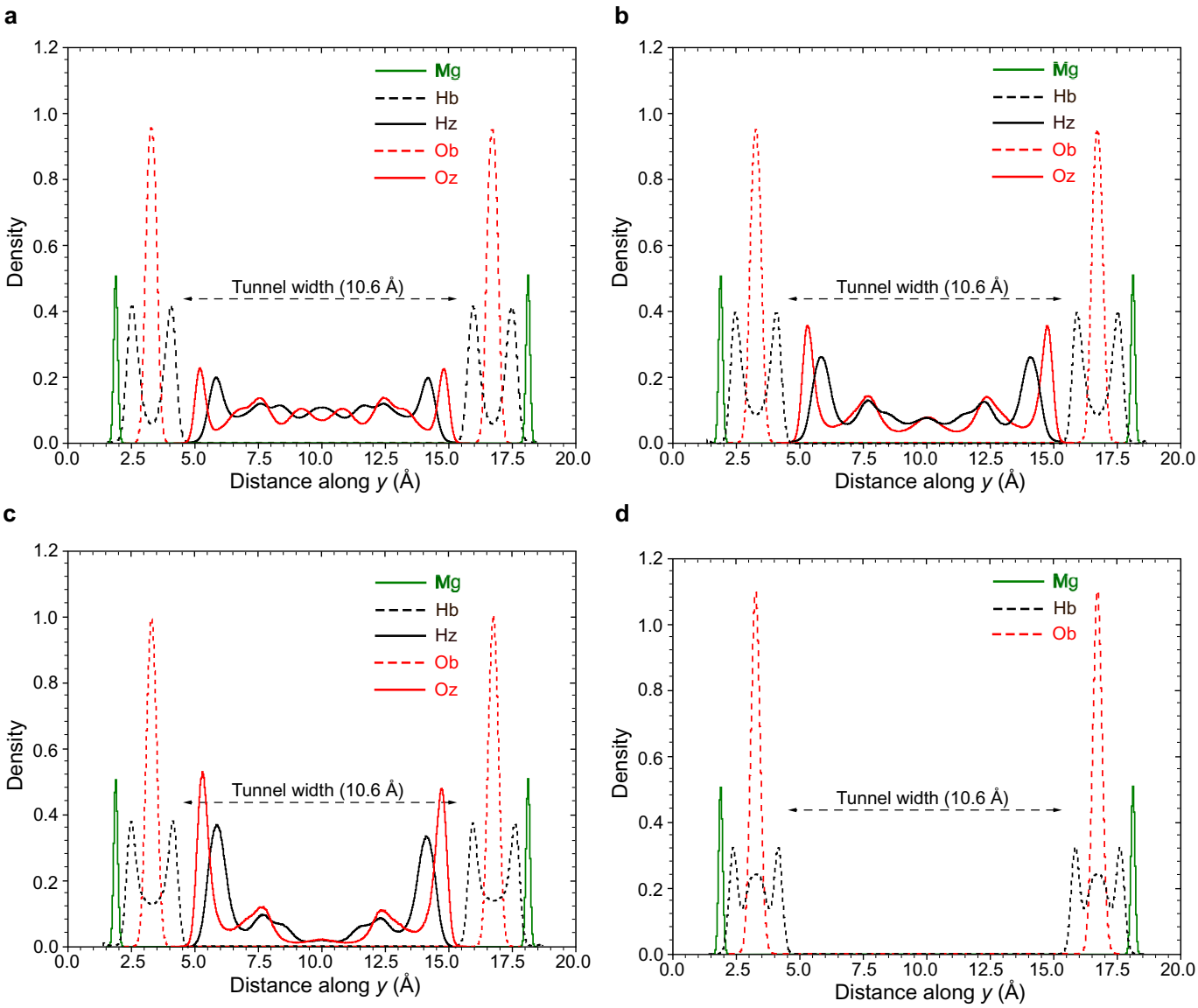

Fig. 7. The atomic density *b*-profile of (a) Sep-8H_2O, (b) Sep-4H_2O, (c) Sep-2H_2O, and (d) Sep-0H_2O. See Table 2 for the description of the abbreviations. See Table 2 for the description of the abbreviations.

H_{b1} mostly interacts with the basal surfaces of the tetrahedral sheets (i.e., top and bottom of the tunnel) (Fig. 5 and Fig. 8). The Zw_1 mainly interacts with the H_{b2} at a distance of 1.12 Å (see Table S4) which is suggestive of a covalent interaction rather than H-bonding. This is likely the most stable Zw that has a weak band at ~3400 cm^{-1} and as persistent up to 200 °C (Fig. 2a).

The second (Zw_2) and third (Zw_3) zeolitic sites are 2.8–3.6 Å, respectively, from the bound water. The 0.8 Å O—O distance between these two waters suggests that both are in constant exchange. Even after long simulation times, both sites never converge to having full occupancy. The fourth zeolitic site (Zw_4) is 5.20 Å from the bound water and represents the farthest zeolitic site from the bound water. At this state, the Zw_4 at each side of the tunnel is bridged by H. The N_{H2O} and L_{H2O} at this zeolitic hydration state are 1.0 and 2.82 Å, respectively (Table 4).

2. *Sep-4H_2O* — In this zeolitic state, there are three zeolitic water sites in the tunnel of sepiolite (Fig. 8b). These sites are 1.30, 4.37 and 6.10 Å from the H_b (see Table S4). The primary difference between this state and Sep-8H_2O is that (i) the Zw_2 is not observed suggesting that this site is the least stable, (ii) the Zw_4 moves to the middle of the tunnel to bridge both Z_w at each side of the tunnel and slightly shifts towards Zw_3 to compensate for the loss of the Zw_2. The Zw_4 slightly shifts downwards in response to the slight collapse in the height of the tunnel (Fig. 8b). The structure of bound water remains mostly the same as in Sep-8H_2O. The Zw_1 still interacts with the H_{b2} at a distance of 1.10 Å. The N_{H2O} and L_{H2O} values at this zeolitic hydration state are 0.66 and 2.86 Å, respectively (see Table S4).
3. *Sep-2H_2O* — In this zeolitic state, there are two zeolitic water sites in the tunnel of sepiolite. The previously observed zeolitic water in the middle of the tunnel does not exist at this stage (Fig. 8c). The zeolitic waters are 1.30 and 3.60 Å from the H_b. The structure of bound water remains the same as in Sep-8H_2O. The Zw_1 still interacts with the H_{b2} at a distance of 1.10 Å. The N_{H2O} and L_{H2O} at this zeolitic hydration state are 0.43 and 2.86 Å, respectively (see Table S4). The loss of water after this state has the most profound effect on the structure of the bound water.

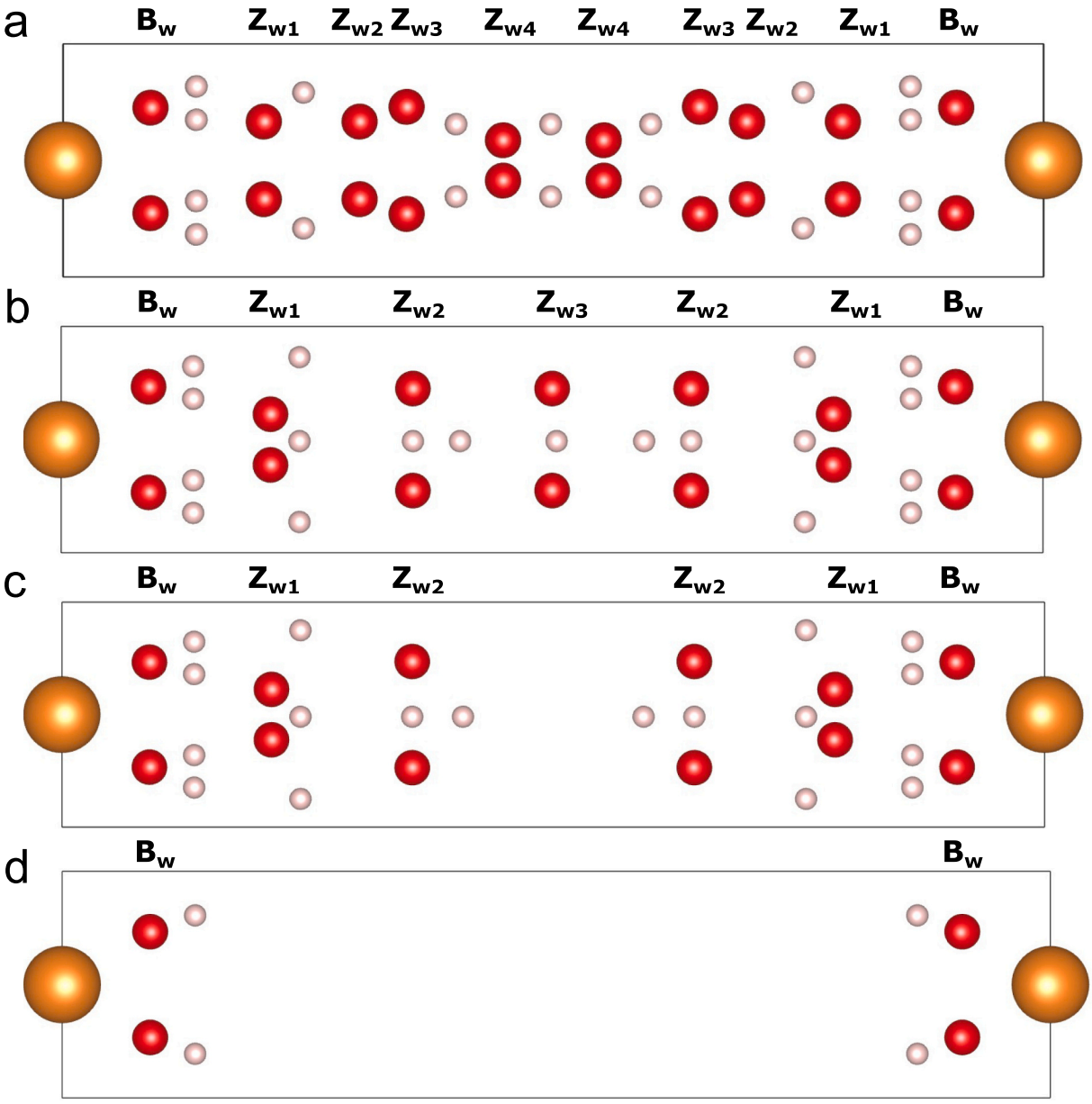

Fig. 8. The idealized sites obtained from MD simulations for zeolitic waters in (a) Sep-8H_2O, (b) Sep-4H_2O, (c) Sep-2H_2O, and (d) Sep-0H_2O.

4. *Sep-0H_2O* — In the absence of zeolitic waters, the structure of the bound water changes significantly (Fig. 8d). The primary change in the structure results from the H_{b2} which is now perpendicular to O_b. This further suggests the importance of the Zw_1 and perhaps explains why it is often necessary to evacuate the tunnel of sepiolite and palygorskite to favor the incorporation of organic molecules into the tunnel.

3.2.3. *Diffusion coefficient of water in the tunnels*

A plot of the mean square displacement of atom types as a function of timestep is shown in Fig. 9. The diffusion coefficient was estimated using the 0 to 1000 ps region of the simulation ($R^2 = 0.996–0.999$). To avoid underestimation of the diffusion coefficient, we considered the diffusion to be 1-D. Indeed, decomposing the diffusion along three axes reveals that over 90% of diffusion occurs along the *c*-axis (see the SI). The 1-D diffusion for water in the tunnel of sepiolite was 5.0×10^{-10} m^2/s for Sep-8H_2O, 3.5×10^{-9} m^2/s for Sep-4 H_2O, and 7.5×10^{-9} m^2/s Sep-2 H_2O, respectively. Previous computational and experimental studies estimate the diffusion coefficient of water in the interlayer of montmorillonite to be between 10^{-9} to 10^{-10} m^2/s depending on the type of interlayer cation and degree of hydration (Flury and Gimmi, 2002; Bourg and Sposito, 2010; Holmboe and Bourg, 2013; Greathouse et al., 2015). The increase in the diffusion coefficient with a decrease in number of zeolitic water molecules is understandable since the higher density in liquids often correlates with higher viscosity, which reduces diffusion of molecules (i.e., Stokes-Einstein relation). Also, the number of H-bonds is reduced as the amount of zeolitic water (Table 4) which facilitates the transport of water within the tunnel.

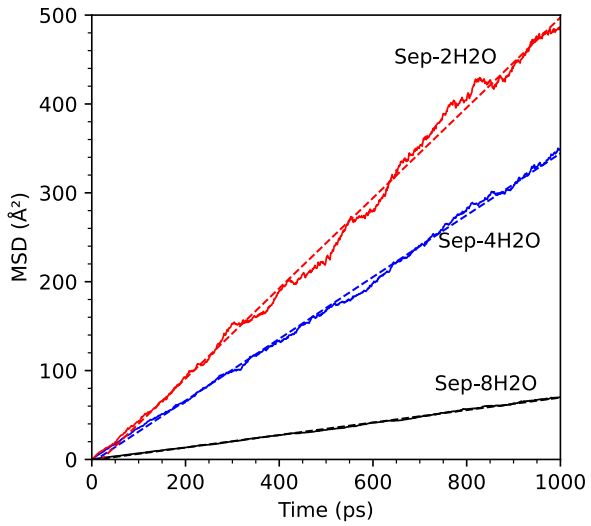

Fig. 9. One-dimensional (along *c*) mean square displacement of zeolitic waters in sepiolite with varying hydration levels.

4. Conclusion

This study provides a comprehensive understanding of the dehydration behavior of sepiolite using a combination of in situ variable-temperature infrared (IR) spectroscopy and classical molecular dynamics (MD) simulations. The IR spectroscopy revealed the distinct thermal stabilities of sepiolite water types: adsorbed water (3252 cm^{-1}) are lost by 100 °C, most zeolitic waters (H_2O, 3375 cm^{-1}) are lost by 100 °C, the residual (most thermally stable) zeolitic waters are lost at >200 °C, and bound water (OH_2, 3616 and 3565 cm^{-1}) remain was mostly impacted at 300 °C, with its subsequent loss driving layer folding. Structural waters (OH, 3690–3674 cm^{-1}) exhibit a systematic red shift, attributed to reduced repulsion from hydrogen atoms of zeolitic water as dehydration progresses, a novel observation correlating with tunnel water content. The MD simulations confirm these findings, showing a ~ 1.2% *a*-axis shrinkage and weakened Si–O–Si bonds (1210 to 1195 cm^{-1}) during dehydration. Zeolitic water organized into 4, 3, and 2 layers in Sep-8H_2O, Sep-4H_2O, and Sep-2H_2O, respectively, with diffusion coefficients increasing (5.0×10^{-10} to 7.5×10^{-9} m^2/s) due to reduced hydrogen bonding (N_{H_2O} decreasing from 1.02 to 0.43). These results highlight the critical role of zeolitic and bound water in the structural dynamics of sepiolite, with the unique red shift distinguishing it from other trioctahedral clays. These findings advance the understanding of the thermal behavior of sepiolite and provide insights into the stability and removal sequences of different water types provide information to guide the tuning of sepiolite for application in catalysis and adsorption through controlled thermal treatment. By understanding how dehydration influences tunnel structure and water mobility, sepiolite can be better engineered for uses such as molecular sieves, gas storage, or as a support for catalysts in environmentally relevant reactions.

CRediT authorship contribution statement

Bidemi T. Fashina: Writing – review & editing, Writing – original draft, Visualization, Validation, Software, Methodology, Investigation, Formal analysis, Data curation, Conceptualization. **Randall T. Cygan:** Writing – review & editing, Supervision, Project administration, Methodology. **Md Wasek Foysal:** Investigation. **Youjun Deng:** Writing – review & editing, Supervision, Methodology, Funding acquisition, Conceptualization.

Declaration of competing interest

There are no conflicts to declare.

Acknowledgements

The authors acknowledge the provision of supercomputing facilities and software by the Texas A&M University High Performance Research Computing (HPRC). The research was financially supported by the Department of Soil and Crop Sciences, Texas A&M University and the Joe and Martha Dixon Endowment.

Appendix A. Supplementary data

Supplementary data to this article can be found online at https://doi.org/10.1016/j.clay.2026.108274.

Data availability

Data will be made available on request.

References

Ahlrichs, J.L., Serna, C., Serratosa, J.M., 1975. Structural hydroxyls in sepiolites. Clays Clay Miner. 23, 119–124. https://doi.org/10.1346/CCMN.1975.0230207.
Allen, M.P., Tildesley, D.J., 2017. Computer Simulation of Liquids. Oxford University Press.
Biovia, D.S., 2018. Material Studio, v. 08. San Diego Dassault Syst.
Bourg, I.C., Sposito, G., 2010. Connecting the molecular scale to the continuum scale for diffusion processes in smectite-rich porous media. Environ. Sci. Technol. 44, 2085–2091.
Brauner, K., Preisinger, A., 1956. Struktur und entstehung des sepioliths. Tschermaks Mineral. Petrogr. Mitteilungen 6, 120–140.
Bukas, V.J., Tsampodimou, M., Gionis, V., Chryssikos, G.D., 2013. Synchronous ATR infrared and NIR-spectroscopy investigation of sepiolite upon drying. Vib. Spectrosc. 68, 51–60. https://doi.org/10.1016/J.VIBSPEC.2013.05.009.
Cygan, R.T., Kubicki, J.D., 2001. Molecular Modeling Theory and Applications in the Geosciences, vol. 42. Rev. Mineral. Geochemistry, Mineral. Soc. Am. Chantilly, Virginia.
Cygan, R.T., Liang, J.-J., Kalinichev, A.G., 2004. Molecular models of hydroxide, oxyhydroxide, and clay phases and the development of a general force field. J. Phys. Chem. B 108, 1255–1266.
Cygan, R.T., Greathouse, J.A., Kalinichev, A.G., 2021. Advances in clayff molecular simulation of layered and nanoporous materials and their aqueous interfaces. J. Phys. Chem. C 125, 17573–17589. https://doi.org/10.1021/ACS.JPCC.1C04600/ASSET/IMAGES/LARGE/JP1C04600_0003.JPEG.
Dejoie, C., Martinetto, P., Dooryhee, E., Brown, R., Blanc, S., Bordat, P., Strobel, P., Odier, P., Porcher, F., Sanchez del Rio, M., 2011. Diffusion of indigo molecules inside the palygorskite clay channels. MRS Online Proc. Libr. 1319, 1–13.
Delgado, S.O., Parladé, J.M.B., Sorando, J.P.C., de Aguayo, F.B.L., 1977. Contribución al conocimiento mineralógico del borde SW de la Cuenca del Tajo (Toledo-San Martín de Pusa). Estud. Geol. 33, 467.
Facey, G.A., Kuang, W., Detellier, C., 2005. Multinuclear magnetic resonance spectroscopy studies of the structuration of the tunnels of sepiolite in the presence of intracrystalline pyridine molecules. J. Phys. Chem. B 109, 22359–22365.
Farmer, V.C., Russell, J.D., 1964. The infra-red spectra of layer silicates. Spectrochim. Acta 20, 1149–1173. https://doi.org/10.1016/0371-1951(64)80165-X.
Fashina, B., Deng, Y., 2022. Smectite, sepiolite, and palygorskite for inactivation of pyocyanin, a biotoxin produced by drug-resistant Pseudomonas aeruginosa. Microporous Mesoporous Mater. 331, 111668. https://doi.org/10.1016/j.micromeso.2021.111668.
Flury, M., Gimmi, T.F., 2002. 6.2 Solute Diffusion. Methods Soil Anal. Part 4 Phys. Methods, 5, pp. 1323–1351.
Fois, E., Gamba, A., Tilocca, A., 2003. On the unusual stability of Maya blue paint: molecular dynamics simulations. Microporous Mesoporous Mater. 57, 263–272.
Ford, W., 2015. Krylov subspace methods. In: Numer. Linear Algebr. With Appl., pp. 491–532. https://doi.org/10.1016/B978-0-12-394435-1.00021-1.
Frost, R.L., Ding, Z., 2003. Controlled rate thermal analysis and differential scanning calorimetry of sepiolites and palygorskites. Thermochim. Acta 397, 119–128.
Frost, R.L., Locos, O.B., Ruan, H., Kloprogge, J.T., 2001. Near-infrared and mid-infrared spectroscopic study of sepiolites and palygorskites. Vib. Spectrosc. 27, 1–13. https://doi.org/10.1016/S0924-2031(01)00110-2.
Fumagalli, L., Esfandiar, A., Fabregas, R., Hu, S., Ares, P., Janardanan, A., Yang, Q., Radha, B., Taniguchi, T., Watanabe, K., Gomila, G., Novoselov, K.S., Geim, A.K., 2018. Anomalously low dielectric constant of confined water. Science (80-.) 360, 1339–1342. https://doi.org/10.1126/science.aat4191.
García-Romero, E., Suárez, M., 2010. On the chemical composition of sepiolite and palygorskite. Clays Clay Miner. 58, 1–20.

García-Romero, E., Suárez, M., Santarén, J., Alvarez, A., 2007. Crystallochemical characterization of the palygorskite and sepiolite from the Allou Kagne deposit. Senegal. Clays Clay Miner. 55, 606–617.
Gionis, V., Kacandes, G.H., Kastritis, I.D., Chryssikos, G.D., 2006. On the structure of palygorskite by mid- and near-infrared spectroscopy. Am. Mineral. 91, 1125–1133. https://doi.org/10.2138/am.2006.2023.
Giustetto, R., Chiari, G., 2004. Crystal structure refinement of palygorskite from neutron powder diffraction. Eur. J. Mineral. 16, 521–532.
Greathouse, J.A., Hart, D.B., Bowers, G.M., Kirkpatrick, R.J., Cygan, R.T., 2015. Molecular simulation of structure and diffusion at smectite-water interfaces: using expanded clay interlayers as model nanopores. J. Phys. Chem. C 119, 17126–17136. https://doi.org/10.1021/ACS.JPCC.5B03314.
Hayashi, H., Otsuka, R., Imai, N., 1969. Infrared study of sepiolite and paly-gorskite on heating. Am. Mineral. J. Earth Planet. Mater. 54, 1613–1624.
Hojati, S., Khademi, H., 2013. Thermal Behavior of a Natural Sepiolite from Northeastern Iran. J. Sci. Islam. Repub. iran 24, 129–134.
Holmboe, M., Bourg, I.C., 2013. Molecular dynamics simulations of water and sodium diffusion in smectite interlayer nanopores as a function of pore size and temperature. J. Phys. Chem. C 118, 1001–1013. https://doi.org/10.1021/JP408884G.
Ilgen, A.G., Leung, K., Criscenti, L.J., Greathouse, J.A., 2023. Adsorption at nanoconfined solid–water interfaces. Annu. Rev. Phys. Chem. 74, 169–191.
Karataş, D., Tekin, A., Çelik, M.S., 2017. Density functional theory computation of organic compound penetration into sepiolite tunnels. Clays Clay Miner. 65, 1–13.
Kuang, W., Facey, G.A., Detellier, C., Casal, B., Serratosa, J.M., Ruiz-Hitzky, E., 2003. Nanostructured Hybrid Materials Formed by Sequestration of Pyridine Molecules in the Tunnels of Sepiolite. https://doi.org/10.1021/cm034867i.
Li, L., Zhuang, G., Li, M., Yuan, P., Deng, L., Guo, H., 2022. Influence of indigo-hydroxyl interactions on the properties of sepiolite-based Maya blue pigment. Dyes Pigments 200, 110138.
Lokanatha, S., Bhattacheijee, S., 1985. Dehydration and phase transformation in sepiolite: α radial distribution analysis study. Zeitschrift für Krist. Mater. 171, 69–80.
Lomoschitz, A., Calvo, J.P., Ordóñez, S., 1985. Sedimentología de las facies detríticas de la Unidad Intermedia del Mioceno al sur y este de Madrid. Estud. Geol. 41, 343–358.
Madejová, J., 2003. FTIR techniques in clay mineral studies. Vib. Spectrosc. 31, 1–10.
Momma, K., Izumi, F., 2011. VESTA 3 for three-dimensional visualization of crystal, volumetric and morphology data. J. Appl. Cryst. 44, 1272–1276. https://doi.org/10.1107/S0021889811038970.
Mora, M., Isabel López, M., Ángeles Carmona, M., Jiménez-Sanchidrián, C., Rafael Ruiz, J., 2010. Study of the thermal decomposition of a sepiolite by mid- and near-infrared spectroscopies. Polyhedron 29, 3046–3051. https://doi.org/10.1016/J.POLY.2010.08.009.
Morikawa, K., Kazoe, Y., Mawatari, K., Tsukahara, T., Kitamori, T., 2015. Dielectric constant of liquids confined in the extended nanospace measured by a streaming potential method. Anal. Chem. 87, 1475–1479.
Nagata, H., Shimoda, S., Sudo, T., 1974. On dehydration of bound water of sepiolite. Clays Clay Miner. 22, 285–291.
Ockwig, N.W., Greathouse, J.A., Durkin, J.S., Cygan, R.T., Daemen, L.L., Nenoff, T.M., 2009. Nanoconfined Water in Magnesium-Rich 2:1 Phyllosilicates. J. Am. Chem. Soc. 131, 8155–8162. https://doi.org/10.1021/ja900812m.
Ogorodova, L.P., Kiseleva, I.A., Vigasina, M.F., Kabalov, Y.K., Grishchenko, R.O., Mel'chakova, L.V., 2014. Natural sepiolite: enthalpies of dehydration, dehydroxylation, and formation derived from thermochemical studies. Am. Mineral. 99, 2369–2373.
Ovarlez, S., Giulieri, F., Chaze, A.M., Delamare, F., Raya, J., Hirschinger, J., 2009. The incorporation of indigo molecules in sepiolite tunnels. Chemistry 15, 11326–11332. https://doi.org/10.1002/chem.200901482.
Pelletier, M., Michot, L.J., Humbert, B., Barrès, O., de la Caillerie, J.-B.D., Robert, J.-L., 2003. Influence of layer charge on the hydroxyl stretching of trioctahedral clay minerals: a vibrational study of synthetic Na-and K-saponites. Am. Mineral. 88, 1801–1808.
Perraki, T., Orfanoudaki, A., 2008. Study of raw and thermally treated sepiolite from the Mantoudi area, Euboea. Greece. J. Therm. Anal. Calorim. 91, 589–593. https://doi.org/10.1007/s10973-007-8329-8.
Petit, S., Decarreau, A., Martin, F., Buchet, R., 2004. Refined relationship between the position of the fundamental OH stretching and the first overtones for clays. Phys. Chem. Miner. 31, 585–592. https://doi.org/10.1007/s00269-004-0423-x.
Post, J.L., Crawford, S., 2007. Varied forms of palygorskite and sepiolite from different geologic systems. Appl. Clay Sci. 36, 232–244. https://doi.org/10.1016/j.clay.2006.10.003.
Post, J.E., Heaney, P.J., 2008. Synchrotron powder X-ray diffraction study of the structure and dehydration behavior of palygorskite. Am. Mineral. 93, 667–675.
Post, J.E., Bish, D.L., Heaney, P.J., 2007. Synchrotron powder X-ray diffraction study of the structure and dehydration behavior of sepiolite. Am. Mineral. 92, 91–97.
Russell, J.D., Fraser, A.R., 1994. Infrared methods. In: Mineralogy, Clay (Ed.), Spectroscopic and Chemical Determinative Methods. Springer Netherlands, Dordrecht, pp. 11–67. https://doi.org/10.1007/978-94-011-0727-3_2.
Sarikaya, Y., Önal, M., Baran, B., Alemdaroğlu, T., 2000. The effect of thermal treatment on some of the physicochemical properties of a bentonite. Clays Clay Miner. 48, 557–562.
Serna, C.J., Vanscoyoc, G.E., 1979. Infrared study of sepiolite and palygorskite surfaces. In: Developments in Sedimentology. Elsevier, pp. 197–206.
Serna, C., Ahlrichs, J.L., Serratosa, J.M., 1975. Folding in sepiolite crystals. Clay Clay Miner. 23, 452–457.
Shinoda, W., Shiga, M., Mikami, M., 2004. Rapid estimation of elastic constants by molecular dynamics simulation under constant stress. Phys. Rev. B 69, 134103. https://doi.org/10.1103/PhysRevB.69.134103.
Shuali, U., Bram, L., Steinberg, M., Yariv, S., 1989. Infrared study of the thermal treatment of sepiolite and palygorskite saturated with organic amines. Thermochim. Acta 148, 445–456. https://doi.org/10.1016/0040-6031(89)85246-3.
Singer, A., 2002. Palygorskite and sepiolite. Soil Mineral. with Environ. Appl. 7, 555–583.
Stukowski, A., 2009. Visualization and analysis of atomistic simulation data with OVITO—the Open Visualization Tool. Model. Simul. Mater. Sci. Eng. 18, 15012.
Teleman, O., Jönsson, B., Engström, S., 1987. A molecular dynamics simulation of a water model with intramolecular degrees of freedom. Mol. Phys. 60, 193–203.
Tilocca, A., Fois, E., 2009. The color and stability of Maya Blue: TDDFT calculations. J. Phys. Chem. C 113, 8683–8687.
Tsampodimou, M., Bukas, V.-J., Stathopoulou, E.T., Gionis, V., Chryssikos, G.D., 2015. Near-infrared investigation of folding sepiolite. Am. Mineral. 100, 195–202.
Wang, Y., 2014. Nanogeochemistry: nanostructures, emergent properties and their control on geochemical reactions and mass transfers. Chem. Geol. 378, 1–23.
Weir, M.R., Kuang, W., Facey, G.A., Detellier, C., 2002. Solid-state nuclear magnetic resonance study of sepiolite and partially dehydrated sepiolite. Clays Clay Miner. 50, 240–247.
Wu, H., He, M., Wu, S., Yang, M., Liu, X., 2022. Near-infrared spectroscopy study of OH stretching modes in pyrophyllite and talc. Crystals 12, 1759.
Yılmaz, M.S., Kalpaklı, Y., Pişkin, S., 2013. Thermal behavior and dehydroxylation kinetics of naturally occurring sepiolite and bentonite. J. Therm. Anal. Calorim. 114, 1191–1199.
Zhou, J., Lu, X., Boek, E.S., 2016. Confined water in tunnel nanopores of sepiolite: Insights from molecular simulations. Am. Mineral. 101, 713–718. https://doi.org/10.2138/am-2016-5430.

Probing Structural Changes of Sepiolite and Zeolitic Water Dynamics with Temperature-Dependent Infrared Spectroscopy and Molecular Simulations

Bidemi Fashina[1,2*], Randall T. Cygan[1], MD Wasek Foysal[1] and Youjun Deng[1*]
btfashi@sandia.gov and yjd@tamu.edu

1. Department of Soil and Crop Sciences, Texas A&M University, College Station, TX 77843-2474, USA
2. Geochemistry Department, Sandia National Laboratories, P.O. Box 5800-0754, Albuquerque, New Mexico 87123, United States

Supplementary Information

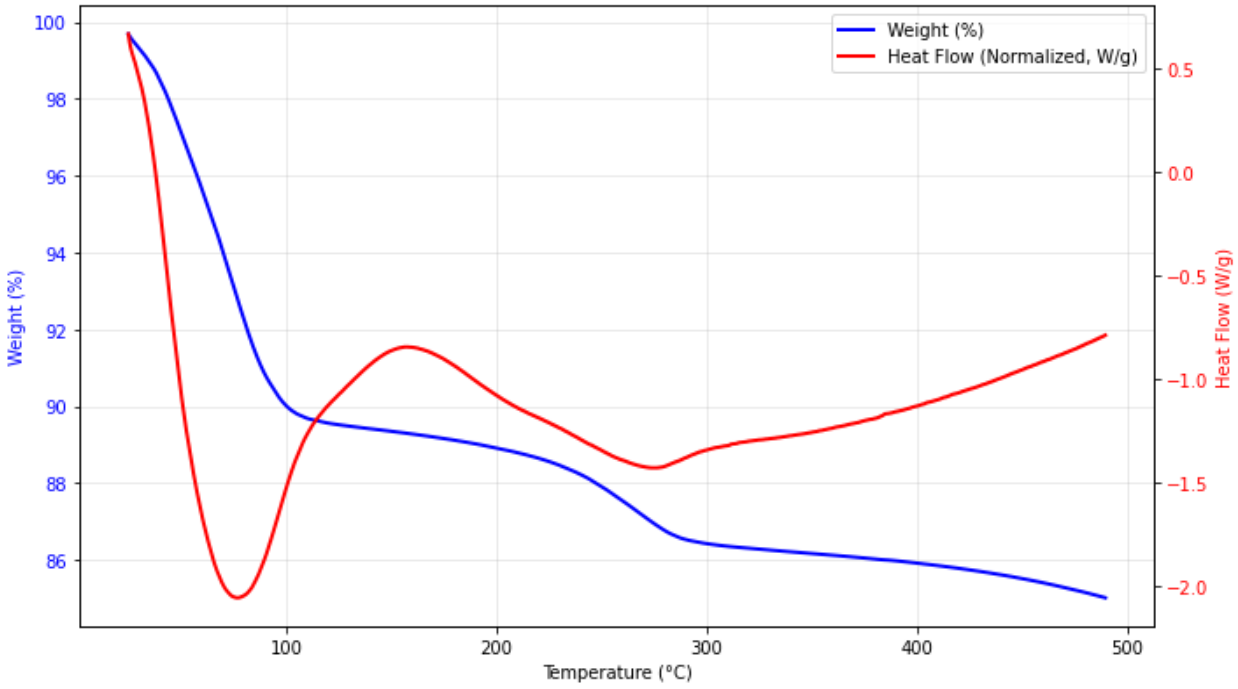

Figure S 1: TGA/DSC of the sepiolite sample

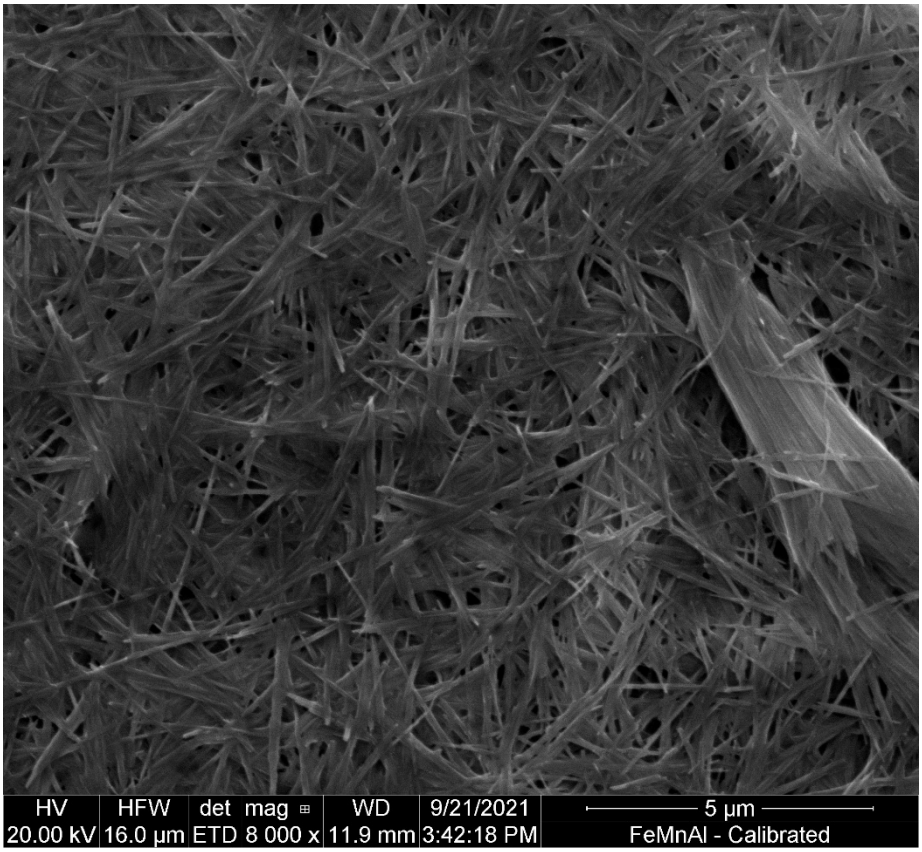

Figure S 2: Scanning Electron Micrograph of sepiolite

Table S 1. Bond Parameters

Harmonic bond strength				k_1	r_o
Forcefield	Species *i*		Species *j*	(kcal/mol Å)	(Å)
SPC	o*		h*	553.9350	1.0000
Harmonic bond-angle bend				k_2	θ_o
	Species *i*	Species *j*	Species *k*		
SPC	h*	o*	h*	45.7696	109.47

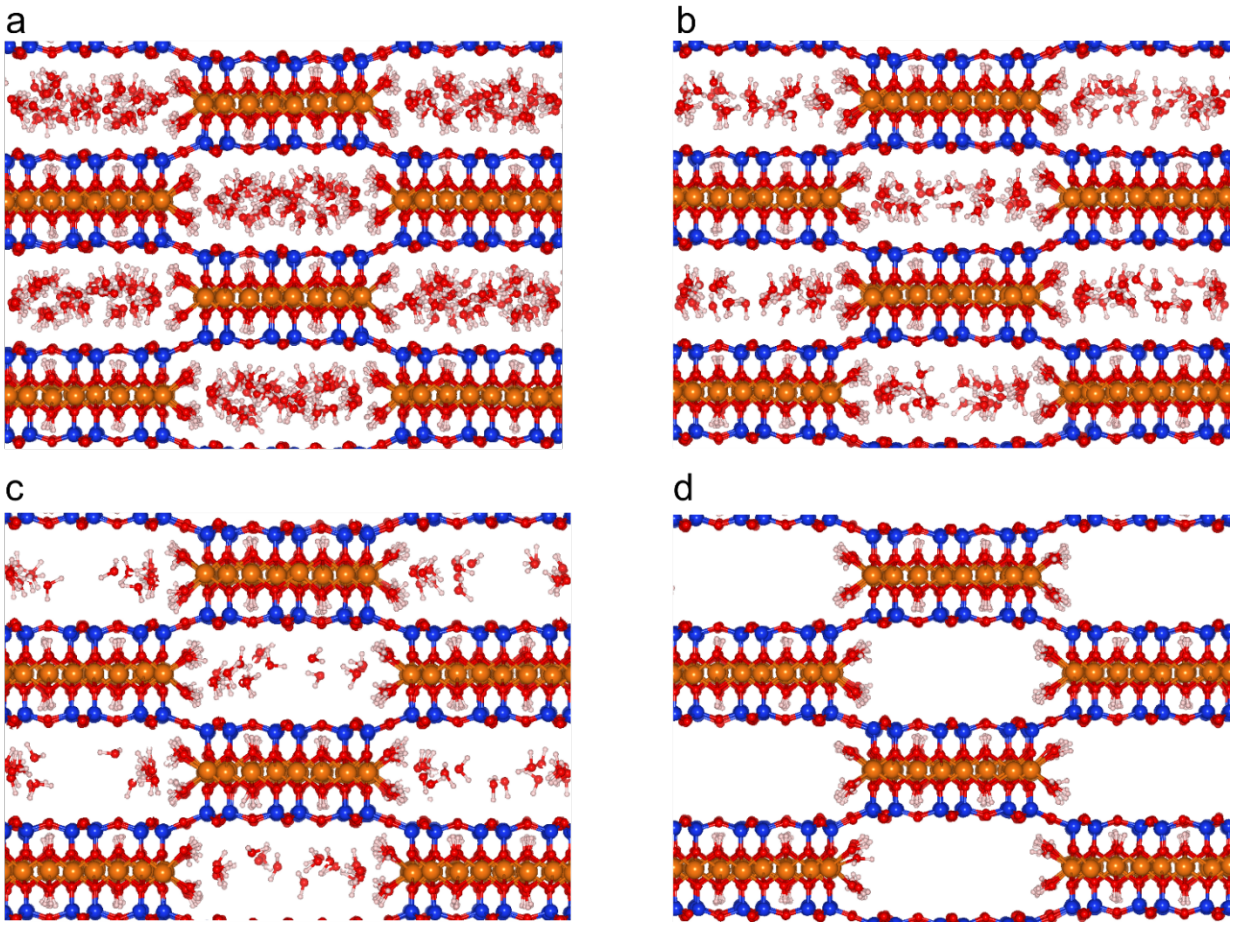

Figure S 3: Cropped snapshots of the models at *NPT* stage of the MD simulation for (a) Sep-8H_2O, (b) Sep-4H_2O, (c) Sep-2H_2O, and (d) Sep-0H_2O,

1. **Post-processing to estimate structural and dynamic properties**

The H-bonding between zeolitic waters were at every 100 timesteps by imposing geometric constrains of 1.2 Å cut-off for maximum O-H covalent bond, 3.5 Å cut-off for maximum O···O distance, an angle cutoff of 130º for minimum O-H···O angle (degrees) and a 2.5 Å maximum H···O distance (Å) for stricter H-bond.

The mean square displacements (MSD, as average of every 100 fs), bond lengths, and bond angles, were computed (as average of every 100 fs) during the second *NVT* run. The two-dimensional self-diffusion coefficient, *D*, in the *yz* plane, was calculated as the slope of the graph of the MSD with time (Cygan and Kubicki, 2001):

$$\langle MSD \rangle^2 = 2Dt + B \qquad 3$$

where 2 is due to two-dimensional diffusion conferred by the geometry of the tunnel. As will be shown later, the diffusion of water in the tunnels of sepiolite is 1-dimensional because the *a*- and *b*-axis are confined.

The trajectories, *d*-spacings (every 100 fs) and radial distribution functions (RDF, as an average of every 100 fs) were computed during the second *NPT* run (Allen and Tildesley, 2017):

$$g(r) = \frac{dn_r}{4\pi r^2 d_{r^*} \rho} \qquad 4$$

Where ρ is the density and dn_r is a function that computes the number of atoms within a shell of thickness *dr*. Pairwise distances were computed for magnesium and oxygen atoms of water (Mg—O_Z), magnesium and the hydroxyl oxygen (Mg—O_h), magnesium and the oxygen atoms in the octahedral sheet (Mg—O_f), and basal oxygens of the tunnels and hydrogen atoms of water (O—H_w). The RDF was calculated from a histogram obtained by binning the pairwise distances in 300 bins from 0.0 to 8 Å.

The atomic density profiles (ADP) were computed from the atomic trajectories and 400 bins to compute histograms. The ADP across (i.e., *a*-axis) and along the length (i.e., *b*-axis) of the tunnel was computed as the distance between an atom *i* and a reference atom *j*. The reference atoms for the ADP across the tunnel are basal oxygen atoms of the tetrahedral sheet of the tunnel while the Mg atoms on the edge/walls of the tunnel are the reference atoms for the ADP along the *b*-axis.

Table S 2. Distance of each atom from the top/bottom of the tunnel

Element	**Distance from the top of tunnel (Å)**			
	n			
	8	**4**	**2**	**0**
O_b	1.05	1.00	1.02	1.03
H_{b1}	0.70	0.66	0.70	0.75
H_{b2}	1.25	1.20	1.20	1.08
H_{z1}	0.80	0.85	0.92	-
H_{z2}		1.62	1.64	-
O_z	1.28	1.36	1.38	-
H_z (bulk-like)	0.47	-	-	-
O_z (bulk-like)	0.42	-	-	-

Table S 3. Distance of each atom from the sides (terminal Mg) of the tunnel

Element	**Distance from the side of tunnel (Å)**			
	n			
	8	**4**	**2**	**0**
O_b	1.45	1.45	1.45	1.45
H_b	2.21	2.19	2.19	1.45/2.19
O_{z1}	3.33	3.47	3.47	
O_{z2}	4.92	5.83	5.80	
O_{z3}	5.70	8.21		
O_{z4}	7.30			
H_{z1}	3.99	3.95	3.95	
H_{z2}	5.68	5.83	6.64	
H_{z3}	6.53	6.61		
H_{z4}	8.18	8.21		

2. Radial distribution functions and coordination numbers (CN)

The distance between the magnesium at the edge of the tunnel and the zeolitic/bound water (i.e., O_w) is 2.13 Å (i.e., Mg—O_W) and the CN is 0.5 irrespective of the degree of zeolitic hydration. The value across the four regimes suggests that irrespective of the content of the zeolitic water, the Mg−O bond distance of bound water is not significantly perturbed by the zeolitic water. The distance between the Mg and framework oxygen (i.e., Mg—O_F) is 2.05 Å while the CN is 4. The distance between the Mg and structural water (i.e., Mg—O_H) is 2.12 Å while the CN is 4. As expected, the degree of zeolitic hydration did not influence these distances. These values are in agreement with previous experimental and computational data (Post et al., 2007; Ockwig et al., 2009).

Table S 4. Bonding length and coordination number

	Mg—O_W		Mg—O_F		Mg—OH	
	BL	CN	BL	CN	BL	CN
Sep-8H_2O	2.11	0.5	2.05	4	2.11	1.5
Sep-4H_2O	2.13	0.5	2.05	4	2.11	1.5
Sep-2H_2O	2.13	0.5	2.05	4	2.11	1.5
Sep-0H_2O	2.13	0.5	2.06	4	2.11	1.5
Experiment [a]	2.06	0.5	2.08	4	2.07	1.5

[a](Post et al., 2007); Mg—O_W = edge Mg and bound water ; Mg—O_F = Mg and oxygen in framework; Mg—OH = Mg and structural OH ; BL = bonding length ; CN = coordination number

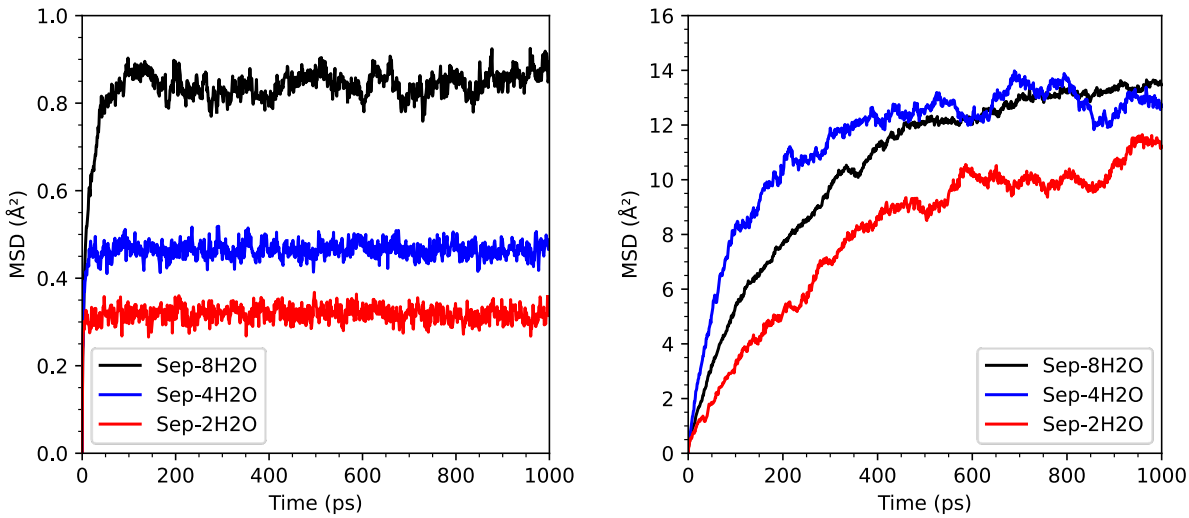

Figure S 4: One dimensional mean square displacement of zeolitic waters in sepiolite with varying hydration levels (a) along *x* and (b) along *y*

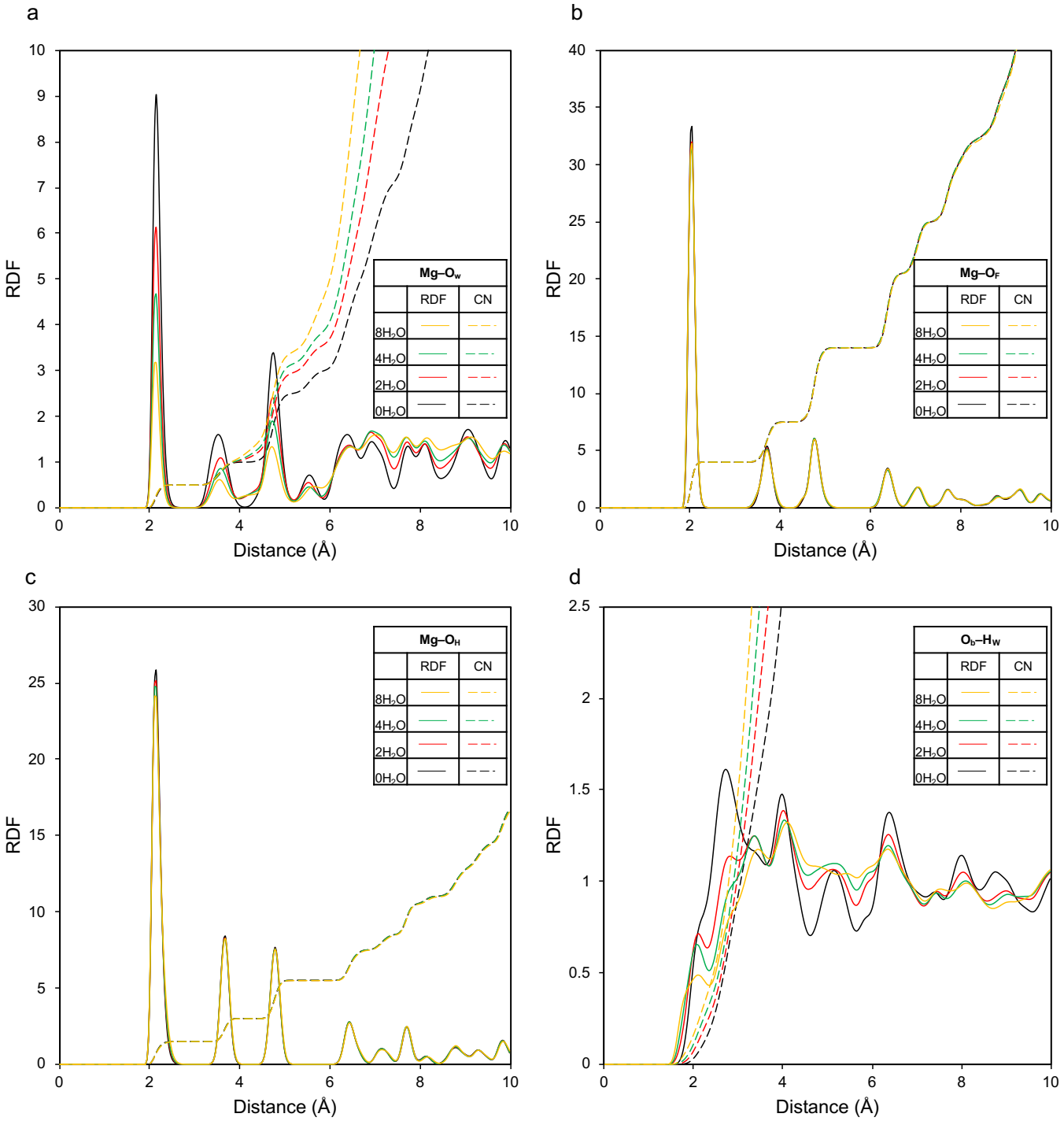

Figure S 5: Radial distribution function of (a) Mg and O_w, (b) Mg and O_f, (c) Mg and O_H, and (d) Ob and H_w. Where O_w is both the oxygen atoms of bound and zeolitic waters, O_f is the oxygen atoms in the octahedral sheet, O_H is the oxygen atoms of the structural waters, O_b is oxygen atoms of the bound waters, and H_w is both the hydrogen atoms of bound and zeolitic waters

References

Allen, M.P., Tildesley, D.J., 2017. Computer simulation of liquids. Oxford university press.

Cygan, R.T., Kubicki, J.D., 2001. Molecular Modeling Theory and Applications in the Geosciences, vol. 42. Rev. Mineral. Geochemistry, Mineral. Soc. Am. Chantilly, Virginia.

Ockwig, N.W., Greathouse, J.A., Durkin, J.S., Cygan, R.T., Daemen, L.L., Nenoff, T.M., 2009. Nanoconfined Water in Magnesium-Rich 2:1 Phyllosilicates. J. Am. Chem. Soc. 131, 8155–8162. https://doi.org/10.1021/ja900812m

Post, J.E., Bish, D.L., Heaney, P.J., 2007. Synchrotron powder X-ray diffraction study of the structure and dehydration behavior of sepiolite. Am. Mineral. 92, 91–97.